The Anatomy of a Continental Tropical Convective Storm

DAVID ATLAS*

NASA Goddard Space Flight Center, Greenbelt, Maryland

CHRISTOPHER R. WILLIAMS

University of Colorado, and NOAA/Aeronomy Laboratory, Boulder, Colorado

(Manuscript received 22 February 2002, in final form 31 May 2002)

ABSTRACT

This study provides a very clear picture of the microphysics and flow field in a convective storm in the Rondonia region of Brazil through a synthesis of observations from two unique radars, measurements of the surface drop size distribution (DSD), and particle types and sizes from an aircraft penetration. The primary findings are 1) the growth of rain by the collision–coalescence–breakup (CCB) process to equilibrium drop size distributions entirely below the 0°C level; 2) the subsequent growth of larger ice particles (graupel and hail) at subfreezing temperatures; 3) the paucity of lightning activity during the former process, and the increased lightning frequency during the latter; 4) the occurrence of strong downdrafts and a downburst during the latter phase of the storm resulting from cooling by melting and evaporation; 5) the occurrence of turbulence along the main streamlines of the storm; and 6) the confirmation of the large drops reached during the CCB growth by polarimetric radar observations. These interpretations have been made possible by estimating the updraft magnitude using the ''lower bound'' of the Doppler spectrum at vertical incidence, and identifying the ''balance level'' at which particles are supported for growth. The combination of these methods shows where raindrops are supported for extended periods to allow their growth to equilibrium drop size distributions, while smaller drops ascend and large ones descend. A hypothesis worthy of pursuit is the control of the storm motion by the winds at the balance level, which is the effective precipitation generating level. Above the 0°C level the balance level separates the small ascending ice crystals from the large descending graupel and hail. Collisions between the two cause electrical charging, while gravity and the updrafts separate the charges to cause lightning. Below the 0°C level, large downward velocities (caused by the above-mentioned cooling) in excess of the terminal fall speeds of raindrops represent the downbursts, which are manifested in the surface winds.

1. Introduction

The nature and evolution of the drop size distribution (DSD) in rain and the relation between the radar reflectivity factor $Z(=\Sigma\, ND^6)$ (N is the number of particles per unit volume, and D is their diameter) and the rainfall rate R have been the subject of extensive studies over the last half century (Fujiwara 1965; Atlas et al. 1999). It has been shown that, given enough time, the DSD may reach an equilibrium functional form by drop collisions, coalescence, and breakup (CCB) in rain entirely below the 0°C level (List et al. 1987; Hu and Srivastava 1995; Ulbrich and Atlas 2002). In this study we use advanced radar techniques to observe the interactions between the microphysics and the kinematics of a storm that are responsible for the development of the equilibrium DSDs. Measurements of the DSD at the surface also provides the associated Z–R relations. The nature of the precipitation process also suggests a relationship to the occurrence of lighting. The unique radar observations provided by a profiler radar and a polarimetric Doppler radar (S-POL) also reveal a number of other previously unreported features of the storm anatomy.

Prior investigators have used either a profiler to examine the air motions and particle types and size distribution of hydrometeors (Williams 2002; Tokay et al. 1999) or polarimetric radar to determine the microphysical properties of storms (Bringi et al. 2002; Zrnic and Ryzhkov 1999; May et al. 2001). Moreover, others have used a combination of airborne and ground-based measurements of drop size distribution to deduce equilibrium forms of the DSD (Atlas and Ulbrich 2000). Conventional radar has also been used to infer the existence of the development of warm rain and ice processes below and above the 0°C level (Szoke and Zipser 1986). A particularly comprehensive investigation (Carey and Rutledge 2000) exploited polarimetric radar and

* Distinguished visiting scientist.

Corresponding author address: David Atlas, Goddard Space Flight Center, Code 912, Greenbelt, MD 20771.
E-mail: datlas@radar.gsfc.nasa.gov

lightning observations to determine the relationship between the nature of the precipitation process and the occurrence of lightning. (The reader is referred to the latter work for other significant references.) In short, pieces of the storm structure, its evolution, and its relation to lightning activity have been known or hypothesized previously. The primary motivation for the present work was the extraordinary clarity of the physical processes of convective precipitation that are illuminated by the profiler, and the synthesis made possible by simultaneous observations with the polarimetric radar and the array of supporting measurements.

The surface disdrometer and profiler observations enable the equilibrium drop size distribution to be identified below the freezing level during the first portion of the storm (section 2). The profiler Doppler velocity spectra enable the balance level to be identified and tracked in the vertical as the updraft moves above the freezing level (section 2c). The downdrafts resolved by the profiler result in a downburst near the surface (section 2d). The S-POL scanning radar corroborates the surface and profiler-observed equilibrium DSDs (section 3). An array of surface lightning detectors observed an increase in lightning after the updraft extended above the freezing level (section 4). The summary (sections 5 and 6) outlines the microphysics and flow field in the convective storm resolved by multiple instruments and suggests methodologies for future analysis strategies.

2. Surface and profiler radar observations

The storm being analyzed in this study passed over the profiler located at the Ji Parana airport (Rondonia, Brazil) on the afternoon of 17 February 1999. While the large-scale easterly wind regime was controlled by the intertropical convergence zone (ITCZ) located to the north of the Rondonia region, this particular storm had a southwest trajectory over the airport. Easterly wind regimes transport more aerosols and higher convective available potential energy (CAPE) air due to the dry continental fetch than westerly wind regimes when the airflow is over the moist, nonaerosol-rich environment of the Amazonia basin (Rickenbach et al. 2002; Williams et al. 2002, hereafter WIL). At noon (1600 UTC), one hour before this storm passed over the airport, there were no precipitating clouds detected by a 10.7-cm polarimeteric radar (S-POL) within 150 km of the airport. At 1700 UTC (1300 LT) approximately 25% of the radar scan domain had reflectivity greater than 25 dB*Z* [dB*Z* are the log units of reflectivity: dB$Z = 10 \log(Z)$]. At this time the closest other cloud system was about 40 km from the airport.

Figure 1a presents the parameters computed from the surface Joss–Waldvogel disdrometer (Joss and Waldvogel 1967). The striking features in Fig. 1a are 1) the large and nearly constant *Z* between 45 and 52 dB*Z*; 2) the extremely large and relatively constant values of the mass-weighted drop diameter D_m of 2 to 3.1 mm; and 3) the rain rate *R* has the same fluctuations as *Z*, ranging between 13 and 20 dB*R* (dB$R = 10 \log R$). The constancy of D_m over the entire range of rain rates indicates a near-constant functional form of the DSD, that is, an *equilibrium drop size distribution* (hereafter equilibrium DSD; List et al. 1987; Hu and Srivastava 1995). When the functional form of the distribution is constant, all of its moments are directly proportional to the number concentration and the rainfall rate *R*. This is the reason for the present finding of the relation $Z = 1260R^{1.04}$, that is, the reflectivity is essentially linear with *R* (Hu and Srivastava 1995; List 1988). Such linear relations were found and explained physically by Atlas and Ulbrich (2000) in a conceptual model based upon surface and aircraft observations of DSD during the Tropical Ocean Global Atmosphere Coupled Ocean–Atmosphere Response Experiment (TOGA COARE). It was this result that motivated us to examine the radar observations in search of a physical understanding of the processes responsible for such behavior.

a. Surface *Z*–*R* relationship

The relationship between *Z* and *R* is commonly determined from the regression of 10 log*Z* on 10 log*R*. To understand the relation of the DSD to the *Z*–*R* relations we use

$$Z = AR^b, \tag{1}$$

where

$$A = cD_m^{2.33}, \quad \text{and} \tag{2}$$

$$b = 1 + 2.33\left[\frac{\Delta \log D_m}{\Delta \log R}\right] \tag{3}$$

(Ulbrich and Atlas 1978; Atlas et al. 1999). The coefficient *c* in Eq. (2) depends upon the functional form of the DSD. When the functional form does not change with *R*, then *c* and D_m are constant, the exponent in Eq. (1) is unity, and *A* is proportional to $(D_m)^{2.33}$. Thus, the larger the mass-weighted diameter, the larger the coefficient *A* in Eq. (1). This explains the large proportionality constant and near unit exponent estimated for the *Z*–*R* relationship found in this storm. The observed large mass-weighted diameter implies the lack of small-sized drops (due to the D^3 dependence of the mass weighting) and the presence of a narrow drop size distribution with modest concentrations. A monodisperse DSD with $D_m = 3.3$ mm (2.5 mm) and concentration of only ≈ 80 m^{-3} (≈ 425 m^{-3}) would account for a reflectivity of 50 dB*Z*.

It is useful to compare the difference in rain rates produced by the present relation $Z = 1260R^{1.04}$ and that resulting from the use of the default relation $Z = 300R^{1.4}$ used by the Weather Surveillance Radar 1988 Doppler (WSR-88D). At 10 log$Z = 45$ dB*Z*, the former results

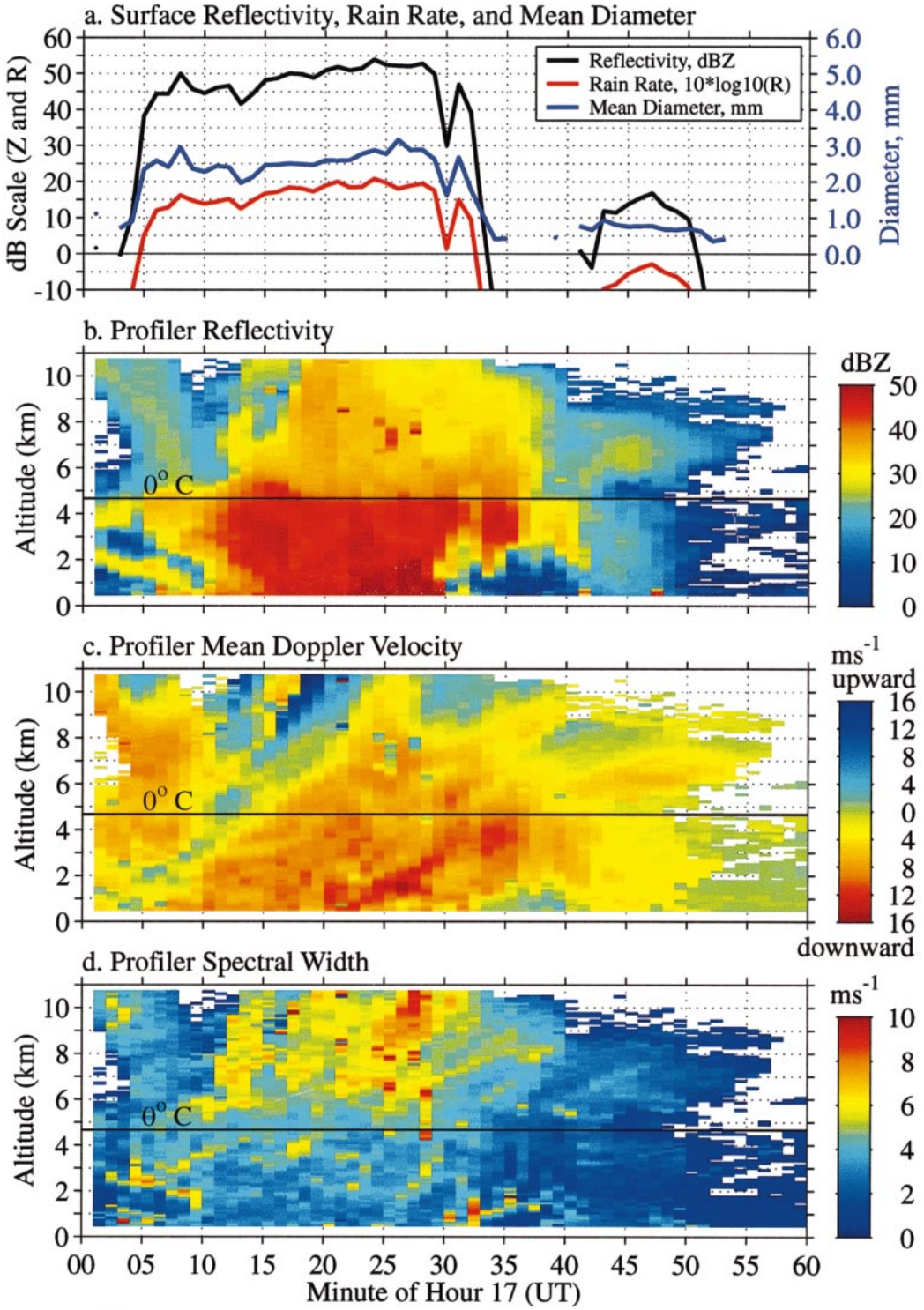

FIG. 1. Surface Joss–Waldvogel disdrometer and profiler radar observations at 1700–1800 UTC 17 Feb 1999. (a) Surface-disdrometer-derived reflectivity (dB$Z = 10 \log Z$), rain rate (dB$R = 10 \log R$), and mass-weighted mean diameter D_m. Here, $D_m = 2.5 \pm 0.5$ mm throughout the period of $Z > 45$ dBZ. (b)–(d) Profiler-measured reflectivity, mean Doppler velocity, and spectral width, respectively. The color scales are on the right. The 0°C level is shown. Reflectivity is 45–50 dBZ up to ≈5 km from 1710 to 1730 UTC. The yellow to red colors on the Doppler velocity panel correspond to downward motions; the green to blues are upward. The draft rises with time and increases in magnitude with altitude. The balance level of zero Doppler velocity corresponds to the blue–green boundary.

in $R = 14.3$ mm h^{-1}, while the latter gives $R = 20$ mm h^{-1}. The rain rates produced by the default relation are overestimated at all $Z < 50.3$ dBZ.

b. Vertical structure of the storm

The vertically pointing profiler observes the vertical structure of the storm as it passes overhead. Figure 1b presents the time–height profiles of the profiler measured reflectivity. The profiler is a fixed vertical pointing Doppler radar operating at 915 MHz with a peak transmitted power of 500 W and beamwidth of 5° (Gage et al. 2000). The reflectivity ranges between 45–50 dBZ between 1708 and 1730 UTC from the surface up to ≈5 km, the height of the freezing level. These reflectivities agree with those measured by the surface disdrometer. Above the 5-km level, the reflectivities decrease sharply to ≈30 dBZ. Notably, there is no evidence of a bright band (Austin and Bemis 1950).

Figure 1c shows the profiler-measured *mean* Doppler velocity. Upward motions are shown in light to dark blue, and downward motions are shown by the yellow to red colors. The mean Doppler velocity is the sum of the reflectivity-weighted particle fall speed and the vertical air motion. The light green boundary (near zero mean Doppler velocity) between the blues and the yellows is the so-called balance level, that is, where the reflectivity of the small number of highly reflective fast-falling large particles is just balanced by a larger number of smaller ones (Atlas 1966). Because of the sixth power weighting of the contributions of the drop diameters to the reflectivity, this is not the balance level for water mass (M), but the two are the same for very narrow DSDs. The broader the DSD, the greater is the ratio of the balance level velocity for Z to that for M. For present purposes we will not make that distinction except where necessary.

In Fig. 1c we see drops rising from near the surface starting at about 1703 UTC and the updraft rises with time. Sequential plan view observations from the S-band (10.7 cm) S-POL radar analysis (NCAR 1999) show that this storm cell is moving at 16 km h^{-1} from 30° (nominally NE). Thus, the updraft is rising toward the NE with a slope of 64° (i.e., 10 km rise over 18 min). Also, the S-POL Doppler measurements indicate a southwesterly flow of 4 to 6 m s^{-1} below 1.5 km, corresponding to a relative flow into the storm of 8 to 10 m s^{-1}. Figure 1c shows that particles are falling out on both sides of the upward column. The particles falling out on the left (SW) of the updraft have smaller Z than those falling out on the right (NE). Thus, we can visualize the column of hydrometeors as a tilted fountain with the smaller particles rising (and growing) in the updraft, while the larger particles fall out on the flanks of the fountain.

The region of net downward motion (yellow to red) between 1708 and 1740 UTC has more internal structure than does the reflectivity field shown in Fig. 1b. The lighter reds are falling at about 8 m s^{-1}, corresponding to reflectivity-weighted drop size of ≈3 mm, in reasonable agreement with surface measurements of drop size. However, one also notes regions of dark red with localized downward speeds exceeding ≈14 m s^{-1}. Since the maximum terminal fall speed of raindrops is 9.6 m s^{-1} at the surface, such speeds indicate localized downdrafts of ≈5 m s^{-1}. It is also interesting that the region of downward motion to the right of the updraft column extends above the 5 km level to a peak altitude of about 8 km at ≈1725 UTC. We shall see later that this is due to a downdraft and not to large, fast-falling particles. We emphasize that this discussion refers only to the mean Doppler speeds. Later we discuss the details contained in the full Doppler velocity spectra.

Figure 1d shows the time–height profile of Doppler velocity spectral width. It is striking that the spectral width is very large above the 5-km freezing level, reaching values in excess of 10 m s^{-1}, and suddenly decreasing to values less than 4 m s^{-1} below 5 km. Moreover, spectral width decreases progressively downward from there to the surface where the spectra are very narrow. For a fixed beam, the total variance of the Doppler spectrum is the sum of the variances due to 1) crosswinds, 2) shear of the radial motions (i.e., the vertical motions of the particles across the beam), 3) turbulence, and 4) the spread of fall speeds of the particles.

Above the 5-km level the largest spectral width is found at the boundaries of the upward and downward motions where the beam intercepts both. These are also regions of large shear, which is also the source of turbulence. From aircraft observations, shear of the vertical drafts is also responsible for the sorting of drops into small and large particles (see Fig. 5 of Stith et al. 2002). Thus shear, turbulence, and particle spectrum width are not separable. However, it is noteworthy that the observations from the Citation aircraft (Stith et al. 2002) show a wide range of frozen particles near the −18°C level (≈8 km altitude). These include relatively large 1-mm ice or graupel (i.e., snow pellets) particles along with a heterogeneous mix of very small ice particles and crystals and correspondingly small fall speed. Thus, in spite of the low reflectivity and small mean fall speed, the spectrum width may be quite large. Also seen in Fig. 1d are ''glitched'' pixels, after 1715 UTC, above the altitude of about 7 km. These broad spectral width signals occur at narrow altitude ranges suggestive of interference from local lightning strikes.

We suggest that the sharp decrease in spectral width below 5 km is due to the change in the particle types and size distribution at this altitude. The presence of the balance level within the core of the updraft indicates that the updraft is acting as a mass spectrometer partitioning the DSD into small and large particles, the latter falling and the former rising. This gives rise to rather narrow distributions of highly reflective narrow distributions of large drops below the updraft maximum (Atlas and Ulbrich 2000). A broad distribution of par-

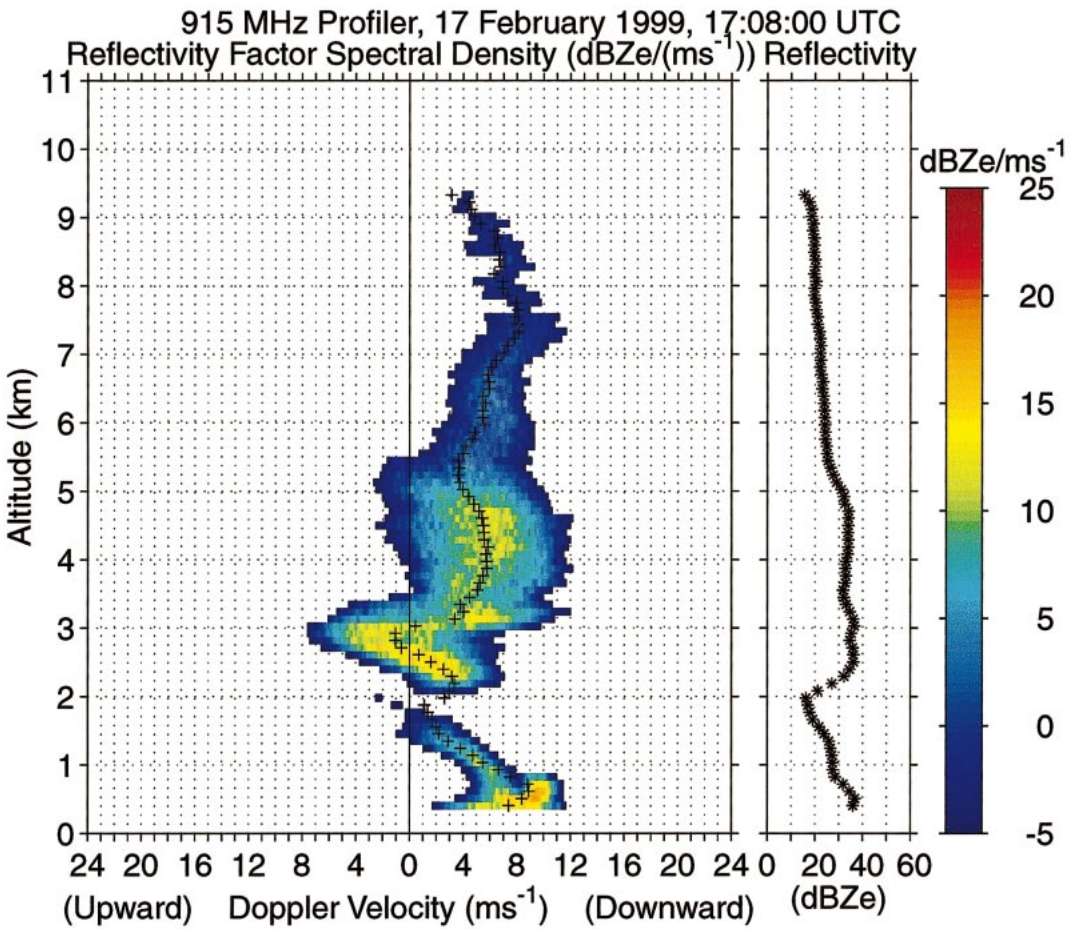

FIG. 2. The vertical profile of reflectivity spectral densities [dBZ (m s^{-1})$^{-1}$] observed at 1708 UTC. Upward motions are to the left of the zero value. The mean Doppler velocity for each spectrum is shown by the crosses, and the total reflectivity at each altitude is shown in the graph to the left of the color bar. The balance level is centered in the updraft ranging from 2.2 to 3.1 km, extending the time of the CCB process leading to equilibrium DSD. The updraft separates the smaller drops from the larger drops that fall out of the updraft. The 10 dBZ decrease in reflectivity from 4.6 to 5.3 km indicates that the CCB growth processes at the warm temperatures dominates the cold processes. The quality control procedure for each spectra consisted of starting from the largest magnitude spectral point and moving down the spectra until the noise floor was reached (Hildebrand and Sekhon 1974). All spectral values from this first noise floor value to the Nyquist velocity were set to the noise floor value. This procedure was performed on both sides of the largest magnitude spectral point in the Doppler velocity spectra. The noise floor values are not plotted in the spectral plots.

ticles is possible above the updraft maximum as the small particles interact in this heterogeneous environment.

c. Profiler radar Doppler velocity spectra

The profiler records the complete Doppler velocity spectra at successive altitudes with a 100-m vertical resolution and 0.16 m s^{-1} spectral resolution over a 21 m s^{-1} Nyquist velocity range. The vertical profile of reflectivity spectral densities [dBZ (m s^{-1})$^{-1}$] observed at 1708 UTC is shown in Fig. 2 with upward motions plotted to the left of the zero value. The crosses on the spectra represent the mean (Z weighted) Doppler velocity (V_z) for each spectrum (also shown in Fig. 1c). The graph to the left of the color bar represents the total reflectivity as a function of height (also shown in Fig. 1b).

Using the so-called lower bound method of Battan (1964) the magnitude of the updraft may be estimated by the peak upward speed. This assumes that the smallest particles have negligible fall speed, a reasonable approximation for drops growing by condensation from cloud base at temperatures warmer than 0°C. In Fig. 2 (1708 UTC) we see that the updraft extends from 2.2 to 3.1 km with maximum speed of about 7 m s^{-1} at 2.8 km. Below 2.8 km, V_z increases sharply downward to about 8 m s^{-1} at the surface. This increase is due to the sloping gradient of V_z seen in Fig. 1c. A mean velocity of 8 m s^{-1} corresponds closely to $D = 3$ mm, very close to the D_m measured by the surface disdrometer. At this time the near-surface spectral width is larger than that

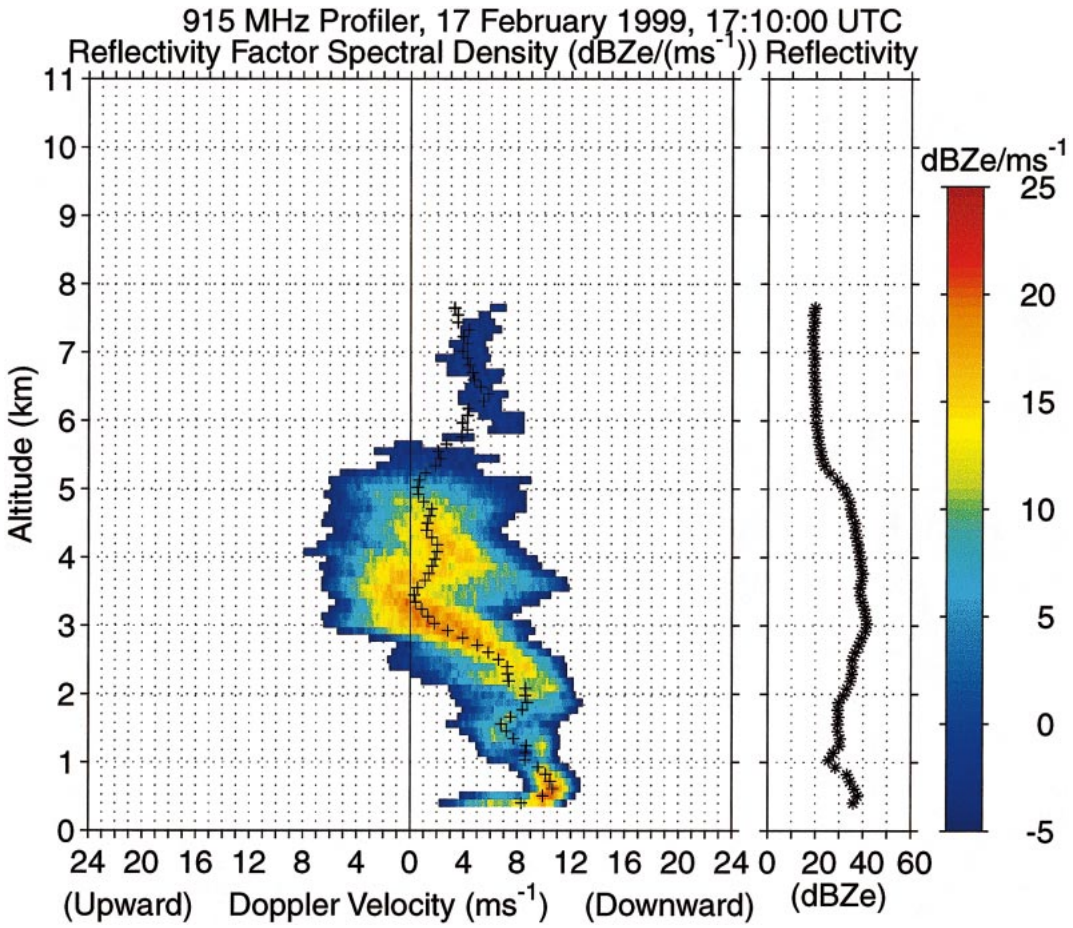

FIG. 3. Similar to Fig. 2, but for the time 1710 UTC. The balance level occurs with an updraft of ≈8 m s^{-1} between 2.8 and 5 km (the 0°C level). The drops are in near balance throughout most of this layer. The mean Doppler velocity below the 2.8-km level ranges between 6 and 11 m s^{-1}, around a mean of about 8 m s^{-1}. This suggests that V_z at the surface corresponds closely to the peak updraft aloft. Values of $V_z > 9.6$ m s^{-1} at the surface are due to downdrafts. Note the decrease of ≈15 dBZ in reflectivity from 4.5 to 5.5 km (across the 0°C level), and the absence of a bright band indicating that the warm processes still dominate the cold processes.

measured at any time during the following 18 min, presumably because it is near the leading edge of the updraft where a range of drop sizes reached the surface simultaneously from different points and times of origin aloft.

The balance level ($V_z \approx 0$) is centered in the core of the updraft ranging from 2.2 to 3.1 km. This means that the raindrops are in near balance with the updraft speed of 7 m s^{-1} thus accomplishing two things. First, the residence time for operation of the collision–coalescence–breakup (CCB) growth process between the drops in balance and those moving either up or down relative to them is extended, thus leading to an equilibrium DSD at smaller rain rates and/or shorter periods than would be the case in the absence of the updraft (Hu and Srivastava 1995; Atlas and Ulbrich 2000). Second, the updraft operates to separate the drops so that the large ones fall while the small ones rise. We then find a narrow distribution of large drops below the balance level consistent with the observations in Fig. 1. Meanwhile the smaller drops rise to freeze and ultimately fall out from higher levels downstream later if they survive evaporation. However, some of the drops that rise above the balance level continue their warm growth and fall out before they freeze; these account for the broad spectral width between 3- and 5-km heights.

It is also noteworthy that the total Z decreases from 34 to 24 dBZ from the altitude of 4.6 to 5.3 km. This indicates that few ice particles exceed the updraft velocity and fall through the 0°C level contributing very little to the total precipitation. In short, the precipitation growth is comprised of two distinct modes: growth by condensation and CCB at warm temperatures and growth by ice processes at cold temperatures; in this profile, the former strongly dominates the latter.

Figure 3 shows the vertical profile of the Doppler velocity spectra at 1710 UTC. The updraft is still about

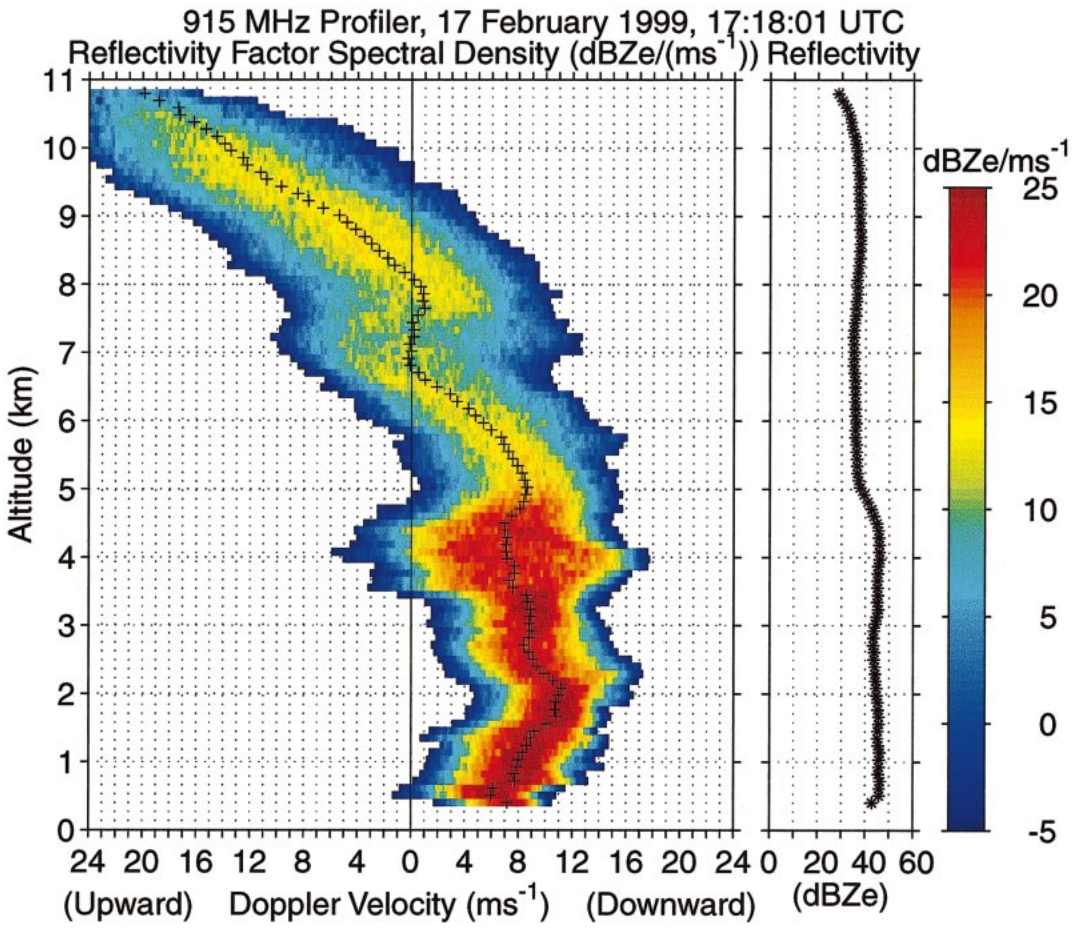

FIG. 4. Similar to Figs. 2 and 3, but for the time 1718 UTC. The updraft extends from 6 to 10.8 km increasing upward to a speed of 24 m s^{-1} at the top level. (The Nyquist velocity was 21 m s^{-1}. The spectra above 9 km were dealiased.) The ice particles are balanced throughout the 6.5–8-km layer in the updraft of 7–9 m s^{-1}. Half of the reflectivity in this layer is found in particles that are *falling*; the maximum fall speeds are 7–9 m s^{-1} relative to the updraft, or absolute speeds of 14–18 m s^{-1}. These particles must be hail of ≈1.5–2 cm diameter. As they leave the base of the updraft below 6 km where $\langle V_z \rangle = 9$ m s^{-1} the largest particles are falling at a speed of 14–17 m s^{-1}. No hail was reported at the surface. The large downward motions result from the negative buoyancy associated with the cooling due to melting and evaporation. As the hail wets in passing through the 0°C level, Z increases by about 9 dBZ. Charge generation due to crystal and hail collisions and charge separation set up lightning activity.

8 m s^{-1}, has risen and broadened in depth, and lies between 2.8 and 5 km. The drops are in near balance throughout most of this layer thus permitting an extended period for the development of an equilibrium DSD. The mean Doppler velocity below the 2.8-km level ranges between 6 and 11 m s^{-1} with a mean of about 8 m s^{-1}. This and other similar observations show that V_z at the surface corresponds closely to the peak updraft aloft. This is reasonable since the updraft must be capable of allowing the growth of drops to sizes that reach the surface. Values of $V_z > 9.6$ m s^{-1} are due to downdrafts. Note again the change in reflectivity ($\Delta Z \approx 15$ dBZ) across the 0°C level at 5 km and the absence of a bright band.

At 1715 UTC the Doppler velocity spectra (not shown) indicate that the top of the updraft has risen to about 7 km, while the base of the updraft remains near 3.8 km. The balance level has risen to 6.7 km where the hydrometeors (as observed by the Citation aircraft; see below) are now primarily small ice crystals of heterogeneous form and frozen droplets of about 1-mm diameter. The primary growth still occurs in the warm updraft region between 3.8 and 5.1 km where $\langle V_z \rangle$ increases downward. Below the base of the updraft at 3.8 km, $\langle V_z \rangle = 9 \pm 0.7$ m s^{-1} all the way to the surface.

d. Updraft extends above the freezing level

The profiler-observed updraft has extended above the freezing level and the storm has entered the cold phase regime. Doppler velocity spectra at 1718 UTC (Fig. 4) show the updraft extending from 6 to 10.8 km increasing upward to the impressive speed of greater than 24 m s^{-1} at the top level. At these higher altitudes, the lower

bound vertical air motion estimates will be biased slightly to larger updrafts (and downdrafts) due to strong horizontal winds spreading the Doppler spectra. With a 5° beamwidth, a 10 m s^{-1} horizontal wind at 11 km increases both ends of the Doppler spectra by about 0.5 m s^{-1}. The ice particles are balanced throughout the 6.5–8-km layer where the updraft ranges between 7 and 9 m s^{-1}. Half of the reflectivity in this layer is due to particles *falling* with terminal fall speeds between ≈7 and ≈14 m s^{-1}, assuming that the maximum downward speed is due in part to evaporative cooling and Doppler spectrum broadening factors. The rapidly descending particles must be hail; spherical hail falling at ≈14 m s^{-1} have diameters of ≈1.5 to 2 cm (Auer 1972; Pruppacher and Klett 1998; Knight and Heymsfield 1983). We use approximations because we have no way of estimating the portion of the downward speed that is due to either cooling or spectrum broadening. Nevertheless, the point is that there must be some moderate to large, fast-falling ice particles such as hail. The aircraft did not observe hail at the −18°C level (≈8 km) at 1811 UTC in an updraft of 7 m s^{-1} after the major updraft had either passed out of the area or had decayed. However, it is unlikely that a narrow hail column would have been traversed along the narrow path sampled by the aircraft.

The rising half of the Doppler spectrum is comprised of small ice crystals and graupel with fall speeds less than the updraft. Thus the conditions are essentially those necessary for noninductive charging by collisions between the descending hail and/or graupel and the ascending smaller ice crystals and the intensification of lightning activity (see below).

Even larger downward velocities are found during the 10-min period subsequent to Fig. 4 (not shown). However, because there was no hail reported at the surface near the profiler site, the hail must have melted. Hail of 2-cm diameter would melt easily in the 5 km of fall below the 0°C level (Rasmussen and Heymsfield 1987). Hence the large downward motions result from the negative buoyancy associated with the cooling due to melting and evaporation. Such downdrafts are indicated by the very large downward velocities (18 to 20 m s^{-1}) below the 3-km level throughout the period 1722–1729 UTC (not shown). The sharp downward decrease in the downdrafts in the lowest 2 to 3 km is turned into a sudden increase in surface wind speed in excess of 8 m s^{-1} and a change in wind direction from SE to NW starting at 1724 UTC (not shown). This was followed by a peak gust of 15 m s^{-1} from the NW at 1732 UTC, which is thought to be the leading edge of the gust front. These sharp changes in surface winds are attributable directly to the strong downdrafts. Thus these observations also depict the conditions that accompany microbursts (Proctor 1988; Srivastava 1987).

In the 1718 UTC observations of Fig. 4 we see that the Z increases by about 9 dBZ as the hail wets in passing through the 0°C level. During this and the following 10 to 12 min, the ice is contributing significantly to the rain rates.

e. Surface disdrometer and profiler radar summary

The key findings using the surface disdrometer and profiler observations are 1) the dominant particle growth occurs almost entirely below the 0°C level between 1700 and 1715 UTC; 2) the major growth takes place where the drops are approximately balanced by the updraft; 3) the near balance of the drops extends the residence time for operation of growth by CCB so that the drop size distribution reaches an equilibrium DSD; 4) the draft also partitions the drops into small particles, which rise and fall out elsewhere if they survive, and large ones, which reach the surface in narrow distributions; 5) the fall speed of the large drops from the base of the updraft to the surface is nearly constant and corresponds approximately to the updraft speed; 6) the latter findings are consistent with a linear Z–R relation having a coefficient that is determined by the large drops, and thus by the maximum updraft aloft; 7) at 1715 UTC the updraft rises above the 0°C level and increases in speed so that one finds ice particles balanced in the 6.5- to 8-km layer where the updraft ranges between 7 and 9 m s^{-1} and the largest downward Doppler velocities of 6–8 m s^{-1}, indicating that particles contributing to half of the reflectivity have absolute fall speeds of ≈9 to 18 m s^{-1}, corresponding to maximum hail size of about 1.5 to 2 cm diameter; 8) we then have collisions between the small rising ice crystals and the falling hail to cause electrical charging and lightning; and 9) cooling by evaporation and melting causes strong downdrafts and downbursts.

3. S-POL scanning radar observations

The S-POL scanning radar observed cross sections of the storm as it passed over the profiler radar. Figure 5 shows the S-POL cross-section structure at 1711 UTC along the 22.8° azimuth, which passes over the profiler located at 41.7-km range. The S-POL radar permits the simultaneous measurement of 1) the radar reflectivity factor Z (shown in color, 2) the mean Doppler velocity along the beam, 3) the Doppler spectral width, and 4) the differential polarization Z_{dr} from which we may deduce the size of D_m. Considerably more information may be gained from either vertical sections at other azimuths and constant altitude plan views of the full field of motion obtained from measurements with two Doppler radars. While not included here for brevity, such fields have been generated. [Analyses performed by L. Carey, S. Rutledge, R. Cifelli, and A. Williams at Colorado State University (2002, personal communication; available online at http://www.olympic.atmos.colostate.edu/lba_trmm/).]

From successive plan view scans of the storm with the S-POL radar, the storm is moving from 30° at a

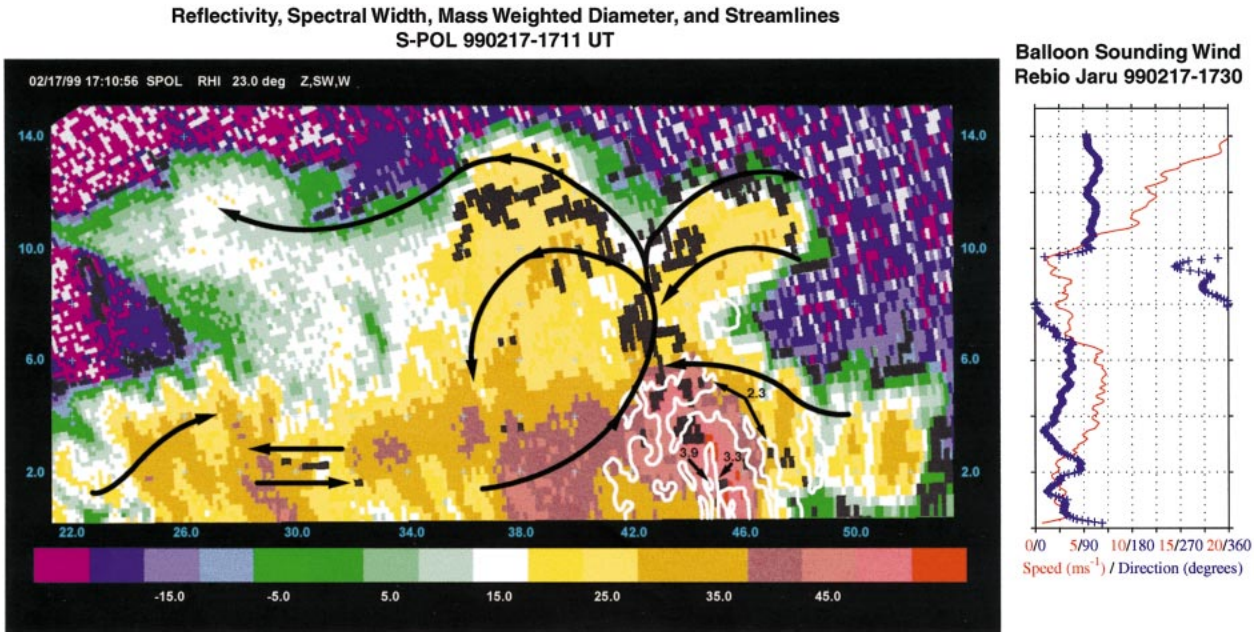

FIG. 5. S-POL radar RHI composite at 1711 UTC, at 22.8° azimuth, which is over the profiler located at the range of 41.7 km. The range shown is between 22 and 60 km. Color is reflectivity with code at bottom. Red region of 45 to 50 dB*Z* up to 5.5-km altitude corresponds to profiler *Z* values between 1710 and 1730 UTC. Streamlines are derived from Doppler measurements. Black pixels are regions of Doppler spectral width in excess of 4 m s^{-1} and follow the streamlines well. White contours are mass-weighted diameters of 2.3, 3.3, and 3.9 mm from differential reflectivity Z_{dr}. The entire high *Z* region is encompassed within the 2.3-mm contour up to the 0°C level and shows that equilibrium DSDs have formed near that level in agreement with the profiler and surface DSD observations.

speed of 16 km h^{-1} (4.4 m s^{-1}). The storm comprises one major rain cell of ≈50 dB*Z* reflectivity, which extends downward from the 5.5-km level. This intense region is ≈4 km wide in range. At a velocity of 16 km h^{-1}, this region passes over the profiler site in ≈15 min in agreement with the duration of the 45- to 50-dB*Z* rain observed by the profiler. Lighter rain of 40 to 45 dB*Z* appears ahead of the intense core. The top of the storm reaches an altitude of 14 km—as deduced from the profiler using the coarser 250-m pulse volume mode (not shown here)—slightly above the nominal tropopause. [Additional profiler observations available online at http://www.al.noaa.gov/WWWHD/pubdocs/TropDyn/TRMM_Precip.html.]

We have deduced the components of the main streamlines along the 22.8° (NNE) direction from the Doppler velocity V_z. The streamlines are essentially vertical where $V_z = 0$; elsewhere the winds correspond closely to the Doppler velocities in the main segment of the storm (at ranges greater than 30 km and heights below 14 km), where the radar beam is nowhere more than 25° off the horizontal. At a range of ≈30 km the wind is from the SSW at 4 to 6 m s^{-1} below 2 km and switches sharply to NNE at 6 m s^{-1} above 2 km ahead of the storm. Relative to the storm motion (4.4 m s^{-1}) the warm low-level air is entering the storm at about 8 to 10 m s^{-1}. The inflow is forced up to become the updraft, also at about 8 to 10 m s^{-1}. The updraft starts to diverge near 8 km into two arms: one toward the NNE at 3 to 6 m s^{-1}, the other toward the SSW at ≈12 m s^{-1}. Another arm of the diverging flow toward the SSW occurs at about 10-km altitude and turns downward to become a downdraft. Because this cross section fails to show the wind components outside of the plane of observation, the updraft strength estimates are crude.

The dual Doppler wind observations provided by the Colorado State University (CSU) Radar Meteorology Research group (not shown) show that the positions of maximum convergence (and thus the maximum updraft) at the 3-km level at 1711 UTC, and that at the 7-km level at 1720 UTC, are located almost exactly above the position of the profiler at the corresponding times. Hence the updraft estimates from the profiler are representative of conditions in the storm core. The dual Doppler observations also show peak updrafts over the profiler ranging from 8 to 15 m s^{-1} between altitudes of 5 and 13 km during the period 1710 and 1730 UTC.

The wind speed and direction as observed by a radio sounding at Rebio-Jaru (about 82 km from the profiler site at 1730 UTC) is shown on the right side of Fig. 5. (The balloon sounding data was provided by Dr. Dev Roy of NASA GSFC.) The winds are light ENE up to about 2 km, turn to NE from there to 5 km, and switch to easterly above 10 km, increasing in strength to about 20 m s^{-1}. The only winds that correspond to the direction of motion of the storm are in the 4- to 6-km layer. Above 10-km altitude the winds cross the 22.8° plane of the range–height indicator (RHI) in Fig. 5 at an angle

of 50° to 60° so that there is a considerable wind component oblique to the plane of observation in Fig. 5 and the cirrus anvil must also spread to the west.

The fact that the direction of motion of the storm corresponds approximately to the winds in the 4- to 6-km layer, within which we find the balance level, is potentially interesting. It has long been known that a precipitation trail moves with the winds at its generating level (Gunn and Marshall 1955). The generating level is that at which the precipitation grows to fallout size. In the present case this occurs at the balance level. Because of the long-standing difficulty in predicting the motion of storms, it would be worthwhile to pursue this hypothesis.

Note also that air from the NNE is entering the storm from the backside at a speed of 9 to 12 m s^{-1} just below the outflow toward the NNE. This backside inflow operates to strengthen the updraft. The region between the upper-level outflow toward the NNE and inflow from that direction just 3 km below is thus marked by strong vertical shear ($\approx$0.003 s^{-1}).

We emphasize that the streamlines and speeds in Fig. 5 represent only those components of the actual three-dimensional wind field in the 22.8° azimuth observation plane.

a. Profiler and scanning radar observations

Both the profiler radar and scanning radar observe the intense rain with reflectivity of $\approx$50 dB*Z* below 5.5 km. The scanning radar shows the shaft of intense rain tilts back toward the NNE from the surface in rough agreement with the time delay of the front of the high intensity rain seen by the profiler. The backward tilt of the rain shaft is also consistent with the NNE outflow in this zone (not shown in Fig. 5).

The black squares in Fig. 5 correspond to Doppler spectral width measurements in excess of 4 m s^{-1}. It is noteworthy that the large spectral width follows the streamlines very well; such a connection has not been reported previously. For a 1° beamwidth a 10 m s^{-1} crosswind would produce spectral width of 0.52 m s^{-1}. Thus the updraft speed itself could not be responsible for the large spectral width there. Rather it is believed that the large values along the updraft are due to turbulence generated by the shear on the draft boundaries. And the large spectral width along the top of the storm is probably due to shear and shear-produced turbulence where the storm outflow meets the high-speed winds (20 m s^{-1}) at the base of the stratosphere.

For present purposes, the most significant results are illustrated by the mass-weighted drop diameters, shown by the white contours in Fig. 5. These are derived from differential reflectivity $Z_{dr} = 10 \log(Z_h/Z_v)$, where ''h'' and ''v'' subscripts represent horizontal and vertical polarization, respectively. The larger the raindrop mass, the greater its ellipticity and the larger is Z_{dr}. The results shown in Fig. 5 are based upon the relation developed recently by Bringi et al. (2002).

In Fig. 5 we show only regions of $D_m \geq 2.3$ mm. At the leading edge of the storm there is also a column of $D_m \geq 3.3$ mm. Such a large D_m implies the presence of a narrow drop size distribution in modest concentrations. It is evident that the entire region of 45 to 50 dB*Z* and surrounding areas in Fig. 5 is comprised of very large drops. Moreover, this large drop region extends up to the 5- to 6-km level indicating that the DSD has reached equilibrium below the 0°C isotherm, entirely by warm growth processes. This is consistent with the finding of equilibrium DSDs at the surface at the profiler site during the entire period of 45–50-dB*Z* reflectivity observed there. This is also implied by the profiler observations of near drop balance in the 3–5-km layer at 1710 UTC in Fig. 3. Only the observations of Carbone and Nelson (1978), Atlas and Ulbrich (2000), and perhaps Testud et al. (2001) imply similar growth processes. All other reports of equilibrium DSDs are based only upon measurements of DSDs at the surface at large rainfall rates.

b. Aircraft in situ observations

The Citation airplane penetrated the storm at the −18°C level ($\approx$3 km above the 0°C level) between 1810 and 1812 UTC after the storm had passed to the southwest of the profiler (Stith et al. 2002). Measurements were made of the size and concentration of hydrometeors between 50 μm and 1 mm, while particle images were observed simultaneously. The aircraft-measured updraft of 4 to 7 m s^{-1} carried large concentrations of small particles ($<\approx$0.3 mm), while the adjacent region of weak downdraft was marked by small concentrations of larger particles, up to $\approx$1 mm diameter. This again illustrates the effect of the drafts in separating the particles by size. But the aircraft either missed the strong updraft that was observed by the profiler earlier, or the draft had decayed. The imager showed a variety of ice crystal types: tiny frozen drops of 30 to 60 μm, plates, capped columns, aggregates up to 0.75 mm, and tiny graupel up to 0.4-mm diameter. The riming or freezing to form the graupel evidently occurred at the lower levels, since no supercooled water was observed at temperatures colder than −7°C. As noted earlier, no hail was found in the aircraft traverse.

4. Lightning production

There is an extensive literature on the storm characteristics required to produce lightning. The most comprehensive recent treatments are those of WIL and Carey and Rutledge (2000). Conventional thinking on the charging mechanism, based in part on field observations and more extensively on laboratory experiments, is summarized by the following statement from WIL.

> The electrification of clouds is caused by collisions of graupel [or hail] and ice crystals in a supercooled cloud (Reynolds et al. 1957; Takahashi 1978; Saunders et al. 1991). The supercooled water supply is maintained by the updraft. The separation of charge occurs by gravity-driven differential motion [and by drafts]. The rate of electrification depends on the rate of these collisions per unit cloud volume. . . .
>
> Both weak updrafts and rapid coalescence [at lower levels] in maritime clouds can in principle result in rapid depletion of their cloud water while growing. When combined with the lack of large graupel, these clouds are missing two ingredients thought to produce charge separation leading to lightning (Lucas et al. 1994; Zipser and Lutz 1994).
>
> The difference in updraft strength above land and ocean surfaces has long been identified as the cause for differences in the cloud microphysical and electrical processes (Rutledge et al. 1992; Zipser and Lutz 1994).

However, Wallace and Hobbs (1977, p. 204, Fig. 4.40) present three variations on this general theme. In particular, their first alternative requires only the collision between rising ice crystals and falling hail. In this case, the hail must have been generated by growth in a supercooled cloud region *prior to* their collisions with the ice crystals. In other words, according to this alternative, supercooled cloud water need not be collocated with the hail. However, in a recent exchange with E. Williams (2002, personal communication), he emphasizes that the rate of charging by the collision mechanism without collocated supercooled water is greatly reduced. If the latter view is accepted, then the apparent absence of supercooled cloud water above the -7°C level as observed by the Citation aircraft (subsequent to the radar observations of Fig. 3) would have to be attributed either to the disappearance of the supercooled water in the 45 to 60 min between the radar and the aircraft measurements or to the failure of the Citation to penetrate the appropriate region. Any further discussion of the charging mechanism is beyond the scope of the present paper. However, it emphasizes the need for in situ experiments of the charging mechanism in real storms.

In the present case, we have shown that the rain grows entirely at warm temperatures (during the period of equilibrium DSDs) prior to 1715 UTC, and then switches sharply to the growth of hail as the updraft rises above the 0°C level. During the warm growth stage there are relatively small concentrations of tiny droplets that are carried up to form the ice particles, and there is no evidence of fast-falling ice particles such as graupel or hail. Thus, this phase of the storm mimics the maritime storms that are noted for the absence of lightning (Zipser and Lutz 1994). It is for this reason that WIL have described the forested areas of Brazil during westerly flow regimes as a ''green ocean'' where convection produces lightning-free storms. The development of rainfall entirely below the freezing level over the sea, which is typical of maritime storms in the Tropics, has been discussed by Szoke and Zipser (1986) among others.

During the second phase of growth (after 1715 UTC) there is clear evidence of large ice particles of about 1.5 to 2 cm with falling speeds of $\approx$15 m s^{-1} through an updraft of $\approx$9 m s^{-1} that carries the small ice crystals upward. This is precisely the environment in which collisional charging and charge separation takes place subject to the caveats discussed above. Hence, this storm is comprised of two stages: 1) a warm rain phase in which lightning is expected to be suppressed, and 2) a cold ice growth phase during which lightning activity is enhanced.

Lightning observations from a network of advanced lightning direction finders provided the time and position of the lightning strokes within $\approx$100 km of the profiler. [The four-station Advanced Lightning Direction Finding (ALDF) network observations were collected by the Global Hydrology and Climate Center at the National Aeronautic and Space Administration (NASA) Marshall Space Flight Center (MSFC), and the observations were processed and provided by Dr. Richard J. Blakeslee at NASA MSFC and Dr. Timothy Lang at Harvard University.] During the period 1700–1715 UTC only 13 lightning strokes were detected within a radius of 20 km of the profiler. In the following 15 min the number of strokes increased sharply to 38 over the same area. While this result is physically plausible we must regard it as a working hypothesis until further experiments confirm it.

5. Further remarks

This study has shown that intense storms in the Tropics over the continents or islands (Carey and Rutledge 2000), and probably in the warm seasons elsewhere, may go through a warm, lightning-poor phase early in their evolution and transition to a cold, lightning-rich phase subsequently. Moreover the warm phase may be marked by the development of an equilibrium drop size distribution and a linear Z–R relation, as observed in the present case and by Atlas and Ulbrich (2000) in the tropical Pacific. However, this appears to occur only when the vertical profile of the updraft is matched to the growth rate of the rain drops in such a manner that the drops can be supported long enough to allow the CCB process to reach equilibrium. More commonly warm rain reaches fallout size before equilibrium is attained. The absence of equilibrium drop size spectra is indicated by the nonlinear relations between radar reflectivity Z and rain rate R as observed in many tropical maritime rains of the Pacific (Tokay and Short 1996) and Atlantic (Hudlow 1979).

Future investigators will find the presence of a balance level helpful in storm diagnostics. When the balance level occurs below the 0°C level precipitation growth occurs entirely in the warm phase by collisions

between the ascending small drops and the descending large ones. Also, there will be no lightning. When the balance level occurs at subfreezing temperatures, particle growth occurs by a combination of deposition of supercooled water, sublimation, and aggregation. The fall speed of the largest particles, and thus their approximate size, may be estimated from the entire width of the Doppler spectrum. When fall speeds correspond to those of graupel or hail, the presence of supercooled water is indicated. Collisions between the ascending small ice particles and descending large ones then generate the electrical charging while gravity and the updraft perform the charge separation necessary for lightning.

A potentially important hypothesis is the apparent control of the storm motion during the warm growth phase by the winds at the balance level. This is the well-known ''generating level'' at which the rain drops first grow to fallout size with a resulting pattern that moves with the winds at that height.

6. Summary

The key findings of this work are as follows.

- The dominant particle growth occurs almost entirely below the 0°C level during the initial phase (i.e., leading edge) of the storm (between 1700 and 1715 UTC).
- The major growth takes place where the drops are approximately balanced by the updraft.
- The near balance of the drops extends the residence time for operation of growth by collision, coalescence, and breakup (CCB) so that the drop size distribution reaches equilibrium.
- The draft also partitions the drops into small particles that rise and fall out elsewhere if they survive, and large ones that reach the surface in narrow distributions.
- The fall speed of the large drops from the base of the updraft to the surface is nearly constant and corresponds approximately to the updraft speed.
- The latter findings are consistent with a linear Z–R relation having a coefficient that is determined by the large drops, and thus by the maximum updraft aloft.
- The appropriate relation is $Z = 1260R^{1.04}$ as compared to the default relation $Z = 300R^{1.4}$ used by the WSR-88D radar. The rain rates produced by the default relation are overestimated at all $Z < 50.3$ dBZ.
- In the later stage of storm, following 1715 UTC, the updraft rises above the 0°C level and increases in speed so that one finds ice particles balanced in the 6.5- to 8-km layer where the updraft ranges between 7 and 9 m s^{-1} and the largest downward Doppler velocities are 6–8 m s^{-1} indicating that particles contributing to half of the reflectivity have absolute fall speeds of ≈9 to 18 m s^{-1} corresponding to maximum hail size of about 1.5- to 2-cm diameter.
- We then have collisions between the small rising ice crystals and the falling hail to cause electrical charging and lightning.
- Cooling by evaporation and melting causes strong downdrafts and downbursts.
- Simultaneous observations with polarimetric and profiler radars show the direct correspondence between the main rain shaft seen by both and validates the existence of an equilibrium drop size distribution throughout that rain column.

Acknowledgments. The work of David Atlas has been supported mainly by the NASA TRMM program. He is particularly indebted to Dr. Ramesh Kakar at NASA Headquarters, and Dr. Franco Einaudi and Mr. Richard Lawrence at Goddard Space Flight Center for continued support and hospitality, and Dr. Joanne Simpson for her inspirational discussions. David Wolff and Jay O'Leary at GSFC were most helpful in generating Fig. 5 and Dev Roy provided the sounding data. The NOAA Aeronomy Laboratory research for the TRMM field campaigns has been supported in part by funding from NASA Headquarters through the NASA TRMM Project Office. The profiler radar analysis was supported in part by NASA Grant NAG5-9753. The authors are also grateful to Professor Carlton Ulbrich of Clemson University, for having computed the equilibrium drop size distributions that triggered this research; to Drs. Richard Blakeslee of NASA Marshall Space Flight Center and Timothy Lang at Harvard University for the lightning data; and especially to Professor Larry Carey (formerly of Colorado State University and now at North Carolina State University) for extensive stimulating discussions.

REFERENCES

Atlas, D., 1966: The balance level in convective storms. *J. Atmos. Sci.,* **23,** 635–651.

——, and C. W. Ulbrich, 2000: An observationally based conceptual model of warm oceanic convective rain in the Tropics. *J. Appl. Meteor.,* **39,** 2165–2181.

——, ——, F. D. Marks Jr., E. Amitai, and C. R. Williams, 1999: Systematic variations of drop size and radar–rainfall relations. *J. Geophys. Res.,* **104** (D6), 6155–6169.

Auer, A. H., Jr., 1972: Inferences about ice nucleation from ice crystal observations. *J. Atmos. Sci.,* **29,** 311–317.

Austin, P. M., and A. C. Bemis, 1950: A quantitative study of the ''bright band'' in radar precipitation echoes. *J. Meteor.,* **7,** 145–151.

Battan, L. J., 1964: Some observations of vertical velocities and precipitation sizes in a thunderstorm. *J. Appl. Meteor.,* **3,** 415–420.

Bringi, V. N., G.-J. Huang, V. Chandrasekar, and E. Gorgucci, 2002: A methodology for estimating the parameters of a gamma raindrop size distribution model from polarimetric radar data: Application to a squall-line event from the TRMM/Brazil campaign. *J. Atmos. Oceanic Technol.,* **19,** 633–645.

Carbone, R. E., and L. D. Nelson, 1978: The evolution of raindrop spectra in warm-based convective storms as observed and numerically modeled. *J. Atmos. Sci.,* **35,** 2302–2314.

Carey, L. D., and S. A. Rutledge, 2000: The relationship between precipitation and lightning in tropical island convection: A C-band polarimetric radar study. *Mon. Wea. Rev.,* **128,** 2687–2710.

Fujiwara, M., 1965: Raindrop-size distribution from individual storms. *J. Atmos. Sci.*, **22,** 585–591.
Gage, K. S., C. R. Williams, P. E. Johnston, W. L. Ecklund, R. Cifelli, A. Tokay, and D. A. Carter, 2000: Doppler radar profilers as calibration tools for scanning radars. *J. Appl. Meteor.*, **39,** 2209–2222.
Gunn, K. L. S., and J. S. Marshall, 1955: The effect of wind shear on falling precipitation. *J. Meteor.*, **12,** 339–349.
Hildebrand, P. H., and R. S. Sekhon, 1974: Objective determination of the noise level in Doppler spectra. *J. Appl. Meteor.*, **13,** 808–811.
Hu, Z., and R. C. Srivastava, 1995: Evolution of raindrop size distribution by coalescence, breakup, and evaporation: Theory and observations. *J. Atmos. Sci.*, **52,** 1761–1783.
Hudlow, M. D., 1979: Mean rainfall patterns for the three phases of GATE. *J. Appl. Meteor.*, **18,** 1656–1669.
Joss, J., and A. Waldvogel, 1967: Ein spektrograph fur niederschlagstropfen mit automatisher auswertung. *Pure Appl. Geophys.*, **68,** 240–246.
Knight, N. C., and A. J. Heymsfield, 1983: Measurement and interpretation of hailstone density and terminal velocity. *J. Atmos. Sci.*, **40,** 1510–1516.
List, R., 1988: A linear radar reflectivity–rainrate relationship for steady tropical rain. *J. Atmos. Sci.*, **45,** 3564–3572.
——, N. R. Donaldson, and R. E. Stewart, 1987: Temporal evolution of drop spectra to collisional equilibrium in steady and pulsating rain. *J. Atmos. Sci.*, **44,** 362–372.
Lucas, C., E. J. Zipser, and M. A. Lemone, 1994: Vertical velocity in oceanic convection off tropical Australia. *J. Atmos. Sci.*, **51,** 3183–3193.
May, P. T., A. R. Jameson, T. D. Keenan, and P. E. Johnston, 2001: A comparison between polarimetric radar and wind profiler observations of precipitation in tropical showers. *J. Appl. Meteor.*, **40,** 1702–1717.
NCAR, 1999: S-POL TRMM-LBA Brazil 1999. S-Pol data user's guide: Introduction. [Available online at http://www.atd.ucar.edu/rsf/TRMM-LBA/.]
Proctor, F. H., 1988: Numerical simulations of an isolated microburst. Part I: Dynamics and structure. *J. Atmos. Sci.*, **45,** 3137–3160.
Pruppacher, H. R., and J. D. Klett, 1998: *Microphysics of Clouds and Precipitation.* Kluwer Academic, 954 pp.
Rasmussen, R. M., and A. J. Heymsfield, 1987: Melting and shedding of graupel and hail. Part II: Sensitivity study. *J. Atmos. Sci.*, **44,** 2764–2782.
Reynolds, S. E., M. Brook, and M. Gourley, 1957: Thunderstorm charge separation. *J. Meteor.*, **14,** 426–436.
Rickenbach, T. M., R. N. Ferreira, J. B. Halverson, D. L. Herdies, and M. A. F. Silva Dias, 2002: Modulation of convection in the southwestern Amazon basin by extratropical stationary fronts. *J. Geophys. Res.*, **107** (D20), 8040, doi: 10.1029/2000JD000263.
Rutledge, S. A., E. R. Williams, and T. D. Keenan, 1992: The Down Under Doppler and Electricity Experiment (DUNDEE): Overview and preliminary results. *Bull. Amer. Meteor. Soc.*, **73,** 3–16.
Saunders, C. P. R., W. D. Keith, and R. P. Mitzeva, 1991: The effect of liquid water on thunderstorm charging. *J. Geophys. Res.*, **96,** 11 007–11 017.
Srivastava, R. C., 1987: A model of intense downdrafts driven by the melting and evaporation of precipitation. *J. Atmos. Sci.*, **44,** 1752–1774.
Stith, J. L., J. E. Dye, A. Bansemer, A. J. Heymsfield, C. A. Grainger, W. A. Peterson, and R. Cifelli, 2002: Microphysical observations of tropical clouds. *J. Appl. Meteor.*, **41,** 97–117.
Szoke, E. J., and E. J. Zipser, 1986: A radar study of convective cells in mesoscale systems in GATE. Part II: Life cycles of convective cells. *J. Atmos. Sci.*, **43,** 199–218.
Takahashi, T., 1978: Riming electrification as a charge generation mechanism in thunderstorms. *J. Atmos. Sci.*, **35,** 1536–1548.
Testud, J., S. Oury, R. A. Black, P. Amayenc, and X. Dou, 2001: The concept of ''normalized'' distribution to describe raindrop spectra: A tool for cloud physics and cloud remote sensing. *J. Appl. Meteor.*, **40,** 1118–1140.
Tokay, A., and D. A. Short, 1996: Evidence from tropical raindrop spectra of the origin of rain from stratiform versus convective clouds. *J. Appl. Meteor.*, **35,** 355–371.
——, ——, C. R. Williams, W. L. Ecklund, and K. S. Gage, 1999: Tropical rainfall associated with convective and stratiform clouds: Intercomparison of disdrometer and profiler measurements. *J. Appl. Meteor.*, **38,** 302–320.
Ulbrich, C. W., and D. Atlas, 1978: The rain parameter diagram: Methods and applications. *J. Geophys. Res.*, **83,** 1319–1325.
——, and ——, 2002: On the separation of tropical convective and stratiform rains. *J. Appl. Meteor.*, **41,** 188–195.
Wallace, J. M., and P. V. Hobbs, 1977: *Atmospheric Sciences: An Introductory Survey.* Academic Press, 467 pp.
Williams, C. R., 2002: Simultaneous ambient air motion and raindrop size distributions retrieved from UHF vertical incident profiler observations. *Radio Sci.*, **37,** 1024, doi: 10.1029/2000RS002603.
Williams, E., and Coauthors, 2002: Contrasting convective regimes over the Amazon: Implications for cloud electrication. *J. Geophys. Res.*, **107** (D20), 8082, doi: 10.1029/2001JD000380.
Zipser, E. J., and K. R. Lutz, 1994: The vertical profile of radar reflectivity of convective cells: A strong indicator of storm intensity and lightning probability? *Mon. Wea. Rev.*, **122,** 1751–1759.
Zrnic, D. S., and A. V. Ryzhkov, 1999: Polarimetry for weather surveillance radars. *Bull. Amer. Meteor. Soc.*, **80,** 389–406.